A SIMPLE ANALYSIS OF DIFFRACTION-LIMITED IMAGING AND SUPER RESOLUTION

L.-J. Gelius, E.G. Asgedom, and M. Tygel

email: *l.j.gelius@geo.uio.no*

keywords: *Diffraction, imaging, super resolution*

ABSTRACT

It is well known that experimental or numerical backpropagation of waves generated by a point-source/-scatterer will refocus on a diffraction-limited spot with a size not smaller than half the wavelength. More recently, however, super-resolution techniques have been introduced that apparently can overcome this fundamental physical limit. This paper provides a simple framework of understanding and analyzing both diffraction-limited imaging as well as super-resolution. By utilizing the null-space solutions of the wave problem, super-resolution is apparently obtained since such solutions can give an extremely well localization of the point-source target.

INTRODUCTION

The diffraction limit in wave physics is well known. Rosny and Fink (2002) have demonstrated experimentally, using ultrasonic waves, that a time reversed wave backpropagates and refocuses at its initial source. In case of a point source the spot size can not be smaller than half the wavelength. Both time-reversal and migration within the integral formulation (like Kirchhoff migration, Schneider 1978) can be represented by the same analytical expression (Esmersoy and Oristaglio, 1988). This theoretical model is further analyzed in this paper employing the general reciprocity theorems introduced by Bojarski (1983). Based on a simple 3-D analysis the cause of the diffraction-limit can be easily explained as a superimposition of a converging and diverging wave as also discussed by Esmersoy and Oristaglio for a 2-D case. This has also been verified experimentally by Rosny and Fink. They introduced in their experiment an acoustic sink in order to collapse the diverging wavefield and obtained super resolution with the time reversed wave focusing to a spot less than 1/14th of the wavelength. Improvement of the image resolution of point like targets beyond the diffraction limit can apparently be obtained employing concepts adapted from conventional statistical multiple signal classification (MUSIC) (Schmidt, 1986). The basis of this approach is the decomposition of the measurements into two orthogonal domains: signal and noise (nil) spaces. Such a decomposition can be obtained by a Singular Value Decomposition (SVD) of the transfer matrix of the actual experiment. Potential applications of the MUSIC approach within radar imaging (Odendaal et al., 1994), microwave breast imaging (Scholz, 2002) as well as within acoustic imaging (Lehman and Devaney, 2003) have been published. Within an acoustic formulation, Lehman and Devaney employed the framework of time-reversal (Prada et al., 2002) to establish a super resolution algorithm. In this paper a simpler and more direct approach is being used to analyze the concept of super resolution. It is demonstrated that by utilizing the null-space solutions of the wave problem, super-resolution is apparently obtained since such solutions can give an extremely well localization of a point-source target.

BASIC FORMULATION

Consider a closed surface S defining a volume V of space as shown in Figure 1, and assume that receivers are distributed evenly across the surface.

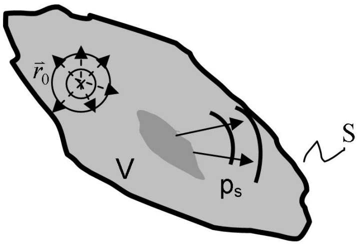

Figure 1: Sketch of problem.

A point source is located inside V at a position $\mathbf{r}_0$ and scatterers are embedded in the (possible) non-uniform background medium. The total wave field p can be described by the scalar inhomogeneous time-reduced Helmholtz wave equation:

$$\nabla^2 p(\mathbf{r},\omega) + k_0^2(\mathbf{r},\omega)p(\mathbf{r},\omega) = -\delta(\mathbf{r}-\mathbf{r}_0) - k_0^2(\mathbf{r},\omega)O(\mathbf{r})p(\mathbf{r},\omega)\ . \tag{1}$$

In Equation 1, k_0 and O are respectively the background wavenumber and the scattering potential defined as:

$$k_0(\mathbf{r},\omega) = \frac{\omega}{c_0(\mathbf{r})},\quad O(\mathbf{r}) = \left[\frac{c_0^2(\mathbf{r})}{c^2(\mathbf{r})} - 1\right]\ , \tag{2}$$

with c and c_0 representing the space-variant velocities of respectively the scatterers and the background medium. In the following, rigorous solutions of Equation 1 will be established employing the technique of Bojarski (1983) which involves Kirchhoff integration of the considered wave-equation over the volume V with the time-retarded and time-advanced Green's function, respectively.

The governing equation for the time-retarded Green's function G_0 of the background medium is given by

$$\nabla^2 G_0(\mathbf{r},\mathbf{r}',\omega) + k_0^2(\mathbf{r},\omega)G_0(\mathbf{r},\mathbf{r}',\omega) = -\delta(\mathbf{r}-\mathbf{r}')\ . \tag{3}$$

Taking the complex conjugate of both sides of Equation 3 yields the corresponding equation for the time-advanced Green's function G_0^*

$$\nabla^2 G_0^*(\mathbf{r},\mathbf{r}',\omega) + k_0^2(\mathbf{r},\omega)G_0^*(\mathbf{r},\mathbf{r}',\omega) = -\delta(\mathbf{r}-\mathbf{r}')\ . \tag{4}$$

Making use of the reciprocity theorems of Bojarski (1983) gives two alternative solutions for the total field:

$$\begin{aligned} p(\mathbf{r},\omega) &= \int_V G_0(\mathbf{r},\mathbf{r}',\omega)\delta(\mathbf{r}-\mathbf{r}_0)dV' + \int_V k_0^2(\mathbf{r}',\omega)G_0(\mathbf{r},\mathbf{r}',\omega)O(\mathbf{r}')p(\mathbf{r}',\omega)dV' \\ &- \int_S \left[\frac{\partial G_0}{\partial n}(\mathbf{r},\mathbf{r}'',\omega)p(\mathbf{r}'',\omega) - G_0(\mathbf{r},\mathbf{r}'',\omega)\frac{\partial p}{\partial n}(\mathbf{r}'',\omega)\right]dS'' \\ &= G_0(\mathbf{r},\mathbf{r}_0,\omega) + \int_V k_0^2(\mathbf{r}',\omega)G_0(\mathbf{r},\mathbf{r}',\omega)O(\mathbf{r}')p(\mathbf{r}',\omega)dV'\ . \end{aligned} \tag{5}$$

and

$$\begin{aligned} p(\mathbf{r},\omega) &= \int_V G_0^*(\mathbf{r},\mathbf{r}',\omega)\delta(\mathbf{r}-\mathbf{r}_0)dV' + \int_V k_0^2(\mathbf{r}',\omega)G_0^*(\mathbf{r},\mathbf{r}',\omega)O(\mathbf{r}')p(\mathbf{r}',\omega)dV' \\ &- \int_S \left[\frac{\partial G_0^*}{\partial n}(\mathbf{r},\mathbf{r}'',\omega)p(\mathbf{r}'',\omega) - G_0^*(\mathbf{r},\mathbf{r}'',\omega)\frac{\partial p}{\partial n}(\mathbf{r}'',\omega)\right]dS''\ . \end{aligned} \tag{6}$$

The contribution from the surface integral in Equation 5 is zero due to radiation conditions as discussed by Bojarski (1983). However, the surface integral in Equation 6 will not cancel out.

FUNDAMENTALS OF BACKPROPAGATION

The fundamentals of the concept of backpropagation can now be discussed and analyzed. First, introduce the scattered field p_s and rewrite Equation 5 as follows:

$$p_s(\mathbf{r},\omega) = p(\mathbf{r},\omega) - G_0(\mathbf{r},\mathbf{r}_0,\omega) = \int_V k_0^2(\mathbf{r}',\omega)G_0(\mathbf{r},\mathbf{r}',\omega)O(\mathbf{r}')p(\mathbf{r}',\omega)dV' \, . \tag{7}$$

which is the so called Lippman-Schwinger equation (Newton, 1982). By measuring this scattered field at receivers evenly distributed along the surface S in Figure 1 (ideal acquisition aperture), the backpropagation operation should ideally give an accurate estimate of the same scattered field at any point inside the volume V. Backpropagation within an integral formulation of migration is described by the Kirchhoff integral (Schneider, 1978; Wiggins, 1984; Langenberg, 1987; Esmersoy and Oristaglio, 1988; Schleicher et al., 2007)

$$p_{bp}(\mathbf{r},\omega) = -\int_S \left[\frac{\partial G_0^*}{\partial n}(\mathbf{r},\mathbf{r}'',\omega)p_s(\mathbf{r}'',\omega) - G_0^*(\mathbf{r},\mathbf{r}'',\omega)\frac{\partial p_s}{\partial n}(\mathbf{r}'',\omega)\right] dS'' \, . \tag{8}$$

For simplicity, often the high-frequency and far-field version of Equation 10 is employed in imaging (i.e. migration)

$$p_{bp}(\mathbf{r},\omega) \approx 2i \int_S \left[k_0(\mathbf{r}'',\omega)G_0^*(\mathbf{r},\mathbf{r}'',\omega)p_s(\mathbf{r}'',\omega)\right] dS'' \, . \tag{9}$$

As shown in Appendix A, extrapolation based on respectively the time-reversal principle or the migration principle gives the same backpropagation result. Hence, evaluation of each of the two focusing techniques can be limited to the discussion of the behavior of the integral in Equation 8 (Esmersoy and Oristaglio, 1988). For an ideal acquisition aperture the surface integral defining the backpropagation of the scattered field can be replaced by an alternative volume integral formulation by combining Equations 7 and 8:

$$\begin{aligned} p_{bp}(\mathbf{r},\omega) &= \int_V k_0^2(\mathbf{r}',\omega)B(\mathbf{r},\mathbf{r}',\omega)O(\mathbf{r}')p(\mathbf{r}',\omega)dV' \, , \\ B(\mathbf{r},\mathbf{r}',\omega) &= -\int_S \left[\frac{\partial G_0^*}{\partial n}(\mathbf{r},\mathbf{r}'',\omega)G_0(\mathbf{r}'',\mathbf{r}',\omega) - G_0^*(\mathbf{r},\mathbf{r}'',\omega)\frac{\partial G_0}{\partial n}(\mathbf{r}'',\mathbf{r}',\omega)\right] dS'' \, . \end{aligned} \tag{10}$$

Comparison between Equations 7 and 10 shows that the background Green's function $G_0(\mathbf{r},\mathbf{r}',\omega)$ is now replaced by the backpropagation kernel $B(\mathbf{r},\mathbf{r}',\omega)$.

By considering the scatterer-free case and ideal aperture an alternative expression can be obtained for the kernel B which also gives more explicit physical insight. Since the left-hand side of both Equations 5 and 6 are equal, by introducing $O = 0$ (e.g. no scatterer) in the same two equations and setting them equal gives the result (also replacing $\mathbf{r}_0$ with $\mathbf{r}'$ without loosing generality):

$$\begin{aligned} B(\mathbf{r},\mathbf{r}',\omega) &= -\int_S \left[\frac{\partial G_0^*}{\partial n}(\mathbf{r},\mathbf{r}'',\omega)G_0(\mathbf{r}'',\mathbf{r}'\omega) - G_0^*(\mathbf{r},\mathbf{r}'',\omega)\frac{\partial G_0}{\partial n}(\mathbf{r}'',\mathbf{r}',\omega)\right] dS'' \\ &= G_0(\mathbf{r},\mathbf{r}',\omega) - G_0^*(\mathbf{r},\mathbf{r}',\omega) \, . \end{aligned} \tag{11}$$

From Equations 10 and 11 it now follows that the kernel B represents backpropagation of data associated with a point source (here located at $\mathbf{r}'$). The right-hand side of Equation 11 can be interpreted as the image obtained at an arbitrary point $\mathbf{r}$ inside V after summation over frequencies (imaging condition). This reconstruction will represent the most optimal result assuming ideal acquisition geometry (i.e. receivers distributed over the complete surface S). Imaging of the point-source is obtained when $\mathbf{r} \rightarrow \mathbf{r}'$, and from the right-hand side of Equation 11 it follows that only a diffraction-limited reconstruction can be obtained due *to the interference between the time-retarded and time-advanced Green's functions*. It is interesting to notice that Equation 11 may also serve as the starting point for both time-reversal (Fink, 1999) and seismic interferometry (Wapenaar, 2004) as briefly discussed in Appendix A.

Theoretically, the diffraction-limit represented by the right-hand side of Equation 11 can be improved by adding to the image the response from an acoustic sink placed at (Rosny and Fink, 2002) (will generate a field which cancels $-G_0^*$). This is not a feasible and practical idea from a computational point of view. However, Rosny and Fink have demonstrated the concept employing experimental data.

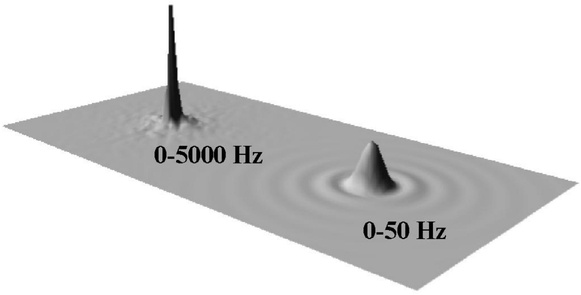

Figure 2: Effect of frequency on the image of the focus.

Considering a homogeneous background it follows from Equation 11 that (again assuming ideal acquisition aperture):

$$\begin{aligned} B(\mathbf{r},\mathbf{r}',\omega) &= G_0(\mathbf{r},\mathbf{r}',\omega) - G_0^*(\mathbf{r},\mathbf{r}',\omega) = \frac{e^{ik_0|\mathbf{r}-\mathbf{r}'|}}{4\pi|\mathbf{r}-\mathbf{r}'|} - \frac{e^{-ik_0|\mathbf{r}-\mathbf{r}'|}}{4\pi|\mathbf{r}-\mathbf{r}'|} \\ &= 2ik_0\,\mathrm{sinc}(\mathrm{k}_0|\mathbf{r}-\mathbf{r}'|)\;, \qquad \mathrm{k}_0 = \frac{\omega}{\mathrm{c}_0} = \frac{2\pi}{\lambda_0}\;, \end{aligned} \tag{12}$$

which gives a focus described by the sinc-function. In Equation 12, k_0 is the wavenumber, c_0 is the velocity of the uniform background medium and λ_0 is the corresponding wavelength. Assuming that the size of the spherical focal spot is mainly defined by the main lobe of the radial sinc-function, its diameter d can be approximated from:

$$d \approx 2|\mathbf{r}-\mathbf{r}'| = \lambda_0\;. \tag{13}$$

The result in Equation 13 is analogous to the focused beam size limit of imaging optics as determined by the diffraction of light. For an axial symmetric optical system the formula of the resolution limit can be obtained from classical diffraction theory for electromagnetic waves, i.e. Rayleigh criterion (Born and Wolf, 1999):

$$\Delta = 0.61\,\lambda_0/NA\;, \tag{14}$$

where Δ is the focused beam size. Moreover, NA is the so called numerical aperture of lens that characterizes the range of angles over which the system can accept or emit light. In the theoretical limit, $NA \to 1$, then $\Delta \to 0.61\,\lambda_0$. Within optics, the diffraction limit can also be explained by a simple diffraction theory for single slit. When a parallel and monochromatic beam is incident on a slit the wave is diffracted and the amplitude of the electromagnetic wave far from the slit can again be described by a sinc function (Born and Wolf, 1999).

By including the available frequency band an improved focus can be obtained as is shown in Figure 2. In the limit of infinite frequencies the focus takes the form of an ideal outward propagating homogenous Green's function (singular at $\mathbf{r} = \mathbf{r}'$):

$$\begin{aligned} \int_{\omega=0}^{\infty} B(\mathbf{r},\mathbf{r}',\omega)d\omega &= \int_{\omega=0}^{\infty} \left[\frac{e^{ik_0|\mathbf{r}-\mathbf{r}'|}}{4\pi|\mathbf{r}-\mathbf{r}'|} - \frac{e^{-ik_0|\mathbf{r}-\mathbf{r}'|}}{4\pi|\mathbf{r}-\mathbf{r}'|}\right] d\omega \\ &= \frac{1}{4\pi|\mathbf{r}-\mathbf{r}'|}\int_{-\infty}^{\infty} e^{i\omega|\mathbf{r}-\mathbf{r}'|/c_0}d\omega = \frac{\delta(|\mathbf{r}-\mathbf{r}'|/c_0)}{4\pi|\mathbf{r}-\mathbf{r}'|}\;. \end{aligned} \tag{15}$$

In Appendix B it is shown that the same result is obtained for an arbitrary background model employing the integral definition of B (cf. Equation 11) in case of an ideal aperture and a high-frequency assumption. Based on this simple analysis of the kernel B in Equation 10, the concept and result of backpropagation can now be better understood. Ideally, the backpropagated field should give an accurate estimate of the true scattered field. However, due to the kernel B in Equation 10 it follows that the backpropagated field

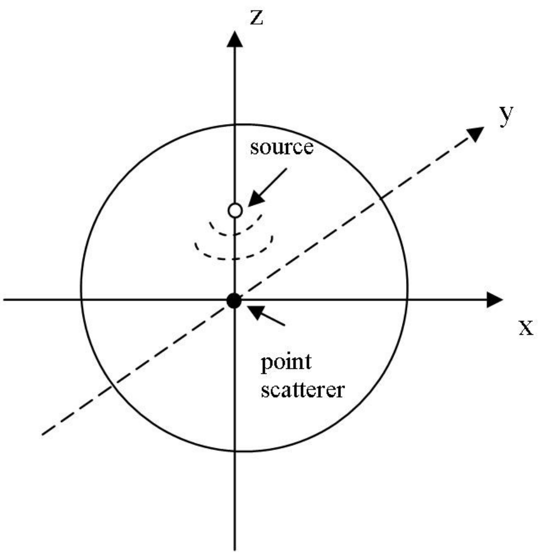

Figure 3: Sketch of simple scattering example.

will contain both causal and non-causal contributions that will interact and give a distorted estimate of the scattered field at the focus point as also discussed by Esmersoy and Oristaglio (1988) for 2-D waves. To illustrate this effect, consider a point scatterer embedded in a homogeneous background and illuminated by a point source as shown in Figure 3.

Figure 4 shows snapshots of the scattered field computed in the vertical plane ($x - z$ plane). In the calculations the homogenous background medium was assigned a velocity of 2000 m/s, the source point was located 200 m above the scatterer along the z-axis and the source pulse was defined by a zero-phase Ricker wavelet with a centre frequency of 20 Hz (the Nyquist frequency was 125 Hz).

It can be seen from the Figure 4 that because of causality (source fired at t=0) no scattered field can exist before the source field illuminates the scatterer (e.g. represented by time frames (a) and (b) in Figure 4). After the scatterer has been illuminated an outward propagating source field is generated. Note that the snapshots in Figure 4 only give a qualitative description of the scattered field due to the fact that each snapshot has been individually scaled.

Assume now that the scattered fields generated in the experiment in Figure 3 are measured at receivers evenly distributed over a sphere surrounding the scatterer (a total number of measurement points 1600 employed here). These fields are then backpropagated using Equation 8, and Figure 5 shows snapshots of the backpropagated field (again individually scaled). The snapshots in Figures 4e and 5e corresponding to a backpropagation time of t=0.160s resemble each other well, but at smaller backpropagation times the differences start to be visible. It can be easily seen from Figure 5 the presence of non-causal contributions in snapshots (a) and (b). The interaction between the causal and non-causal wavefields in Figure 5 also causes the focused wave to be diffraction-limited as shown in snapshot (c) (compare with snapshot (c) in Figure 4). The size of the focal spot in Figure 5c is in the order of half of the centre wavelength as expected. Note also the polarity change between the converging and diverging waves in 5 in accordance with predictions from the theory (cf. Equation 11).

Until now a perfect acquisition surface has been assumed, which implies evenly distributed receivers across the closed surface S (being a sphere in the example considered here). However, if the aperture is limited the backpropagated field represents an even more distorted version of the true scattered field. Figure 6(a)-c shows an example with receivers only placed along the right part of a ring in the vertical slice through the surface of the sphere (cf. Figure 3). The corresponding snapshots show a more complex wave focus (caused by treating a 3-D problem as a two-dimensional one). Again the wave focus is formed by the interaction of converging and diverging waves and is more distorted than the focus obtained in the ideal aperture case (cf. Figure 5).

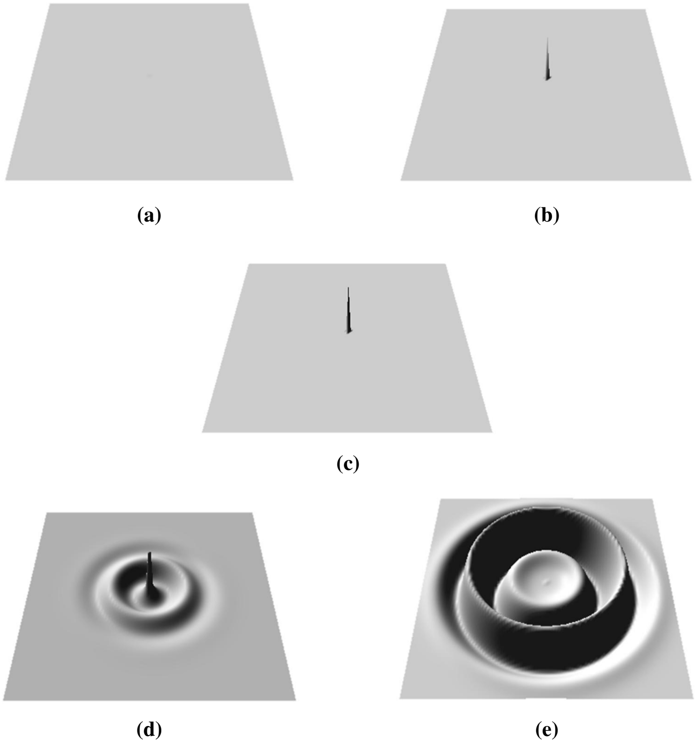

Figure 4: Snapshots showing the scattered field from a point scatterer at different propagation times: (a) t=0.040s, (b) t=0.068s, (c) t=0.096s, (d) t=0.132s and (e) t=0.160s.

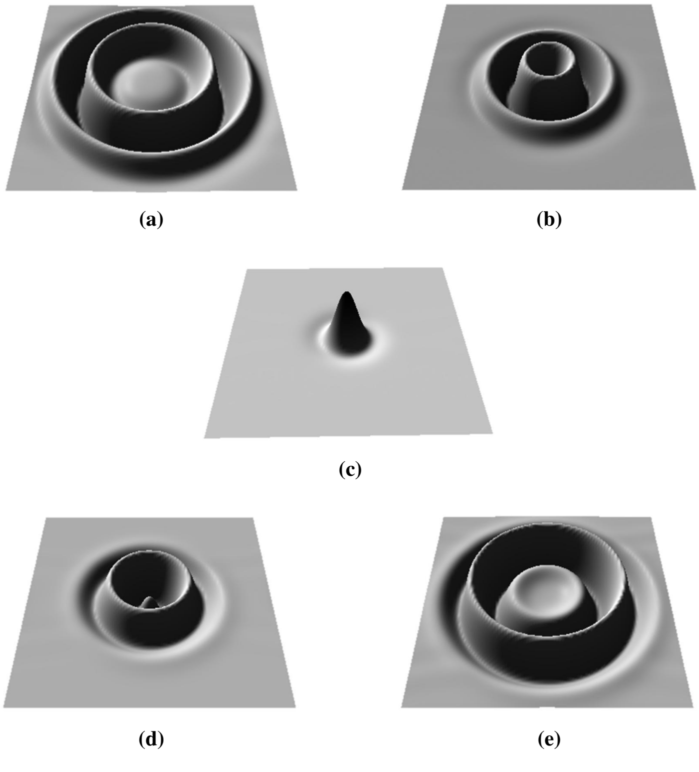

Figure 5: Snapshots of backpropagated field (complete acquisition aperture) at different backpropagation times: (a) t=0.040s, (b) t=0.068s, (c) t=0.096s, (d) t=0.132s and (e) t=0.160s.

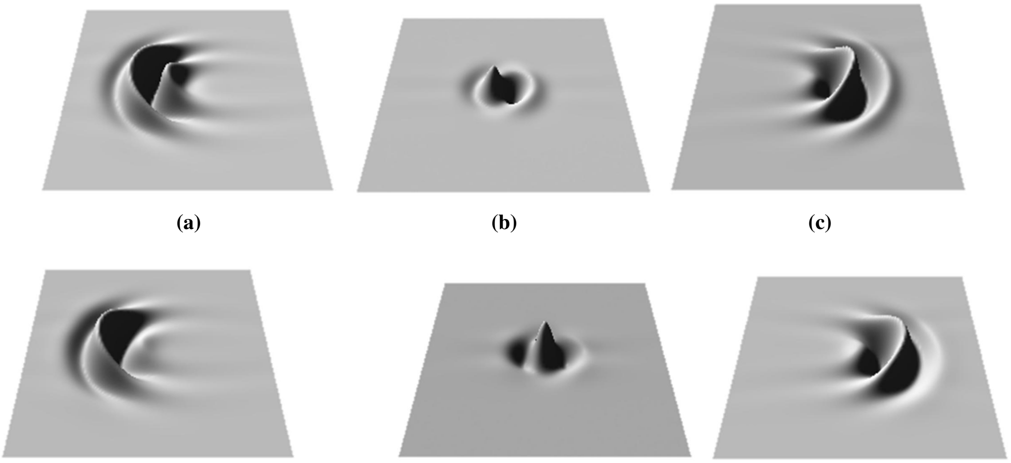

(a) (b) (c)

(d) (e) (f)

Figure 6: Snapshots of backpropagated field (limited aperture - half-ring) at different (back)propagation times: (a) and (d) t=0.068s, (b) and (e) t=0.100s, (c) and (f) t=0.132s. Employing, respectively, Equation 16 (upper row) and Equation 17b (lower row).

For the numerical example considered here the high-frequency and far-field version of the backpropagation operation as given by Equation 9 is valid. Within such an assumption and imposing again an ideal acquisition aperture it then follows from Equations 10 and 11 that

$$\begin{aligned} p_{bp}(\mathbf{r},\omega) &= -\int_S \left[\frac{\partial G_0^*}{\partial n}(\mathbf{r},\mathbf{r}'',\omega) p_s(\mathbf{r}'',\omega) - G_0^*(\mathbf{r},\mathbf{r}'',\omega)\frac{\partial p_s}{\partial n}(\mathbf{r}'',\omega)\right] dS'' \\ &\approx 2i\int_S k_0(\mathbf{r}'',\omega) G_0^*(\mathbf{r},\mathbf{r}'',\omega) p_s(\mathbf{r}'',\omega) dS'' \approx \int_V k_0^2(\mathbf{r}',\omega) B(\mathbf{r},\mathbf{r}',\omega) O(\mathbf{r}') p(\mathbf{r}',\omega) dV' \ , \\ & B(\mathbf{r},\mathbf{r}',\omega) = G_0(\mathbf{r},\mathbf{r}',\omega) - G_0^*(\mathbf{r},\mathbf{r}',\omega) \ . \end{aligned} \tag{16}$$

A more heuristic form of backpropagation or migration is to employ the simple matched filtering approach

$$p_{bp}^m(\mathbf{r},\omega) = \int_S G_0^*(\mathbf{r},\mathbf{r}'',\omega) p_s(\mathbf{r}'',\omega) dS'' \ . \tag{17a}$$

Equation 17a can be further elaborated on making use of Equation 16 (ideal aperture):

$$\begin{aligned} p_{bp}^m(\mathbf{r},\omega) &= \int_S G_0^*(\mathbf{r},\mathbf{r}'',\omega) p_s(\mathbf{r}'',\omega) dS'' = \int_V k_0^2(\mathbf{r}',\omega) B_m(\mathbf{r},\mathbf{r}',\omega) O(\mathbf{r}') p(\mathbf{r}',\omega) dV' \ , \\ B_m(\mathbf{r},\mathbf{r}',\omega) &= G_m(\mathbf{r},\mathbf{r}',\omega) + G_m^*(\mathbf{r},\mathbf{r}',\omega), \quad G_m(\mathbf{r},\mathbf{r}',\omega) = \frac{1}{2ik_0(\mathbf{r}',\omega)} G_0(\mathbf{r},\mathbf{r}',\omega) \ . \end{aligned} \tag{17b}$$

Hence, in this case the focus is formed by the interference sum of a converging and diverging wave governed by the new kernel B_m. Even for a limited acquisition case one should therefore expect the diverging and converging waves having the same polarity when employing Equation 17b. This is different from the case when employing Equation 16 where the two interfering waves have opposite polarity. This phenomenon can be clearly observed in Figure 6 (compare (a)-(c) with (d)-(f)). For this limited-view example, the focus seemed to have improved in case of matched filtering.

IMAGING BEYOND THE DIFFRACTION-LIMIT - SUPER RESOLUTION

The question is now if diffraction-limited imaging (focusing) can be somehow relaxed by introducing alternative approaches to image formation. Traditional imaging makes direct use of the signal part of the measurements. Alternatively, identification of the orthogonal noise or nil space apparently can give super resolved point scatterers where the size of the focus is represented by fractions of a wavelength (Lehman and Devaney, 2003). However, closer analysis shows that the output from such a method has to be interpreted as an extreme localization map of a point target rather than a conventional image. The key to this super-resolved localization is to decompose the measurements into a signal space and a complementary noise (nil) space. Such a decomposition is obtained employing a SVD analysis of the data set. The original work of Lehman and Devaney derive the main results within the frame work of time reversal. In this paper an alternative approach is employed which provides a more direct and simpler analysis of the problem.

Assume now limited acquisition geometry so that receivers (and active sources) no longer are distributed on a closed surface surrounding the scatterer, but fall along separate (or coincident) source- and receiver-arrays. Let N represent the total number of receivers and M the total number of sources. Due to this limited acquisition geometry, one should expect an image far from that of the ideal diffraction-limited case shown in Fig 5(c). For a fixed source ($\mathbf{r}^s$) - receiver ($\mathbf{r}^r$) pair, the field scattered from a perturbation $O(\mathbf{r})$ inside the volume V in Figure 1 is described by the Lippman-Schwinger equation. Assuming Born scattering and a point scatterer (secondary source) with strength O_m located at $\mathbf{r}_m$ this implies (by analogy with Equation 7):

$$\begin{aligned} p_s(\mathbf{r}^r,\omega) &= \int_{\mathbf{r}'\in V} k_0^2(\mathbf{r}',\omega)G(\mathbf{r}^s,\mathbf{r}',\omega)O(\mathbf{r}')G(\mathbf{r}^r,\mathbf{r}',\omega)d\mathbf{r}' \\ &= \int_{\mathbf{r}'\in V} k_0^2(\mathbf{r}',\omega)G(\mathbf{r}^s,\mathbf{r}',\omega)O_m\delta(\mathbf{r}'-\mathbf{r}_m)G(\mathbf{r}^r,\mathbf{r}',\omega)d\mathbf{r}' \\ &= k_0^2(\mathbf{r}_m,\omega)O_mG(\mathbf{r}^s,\mathbf{r}_m,\omega)G(\mathbf{r}^r,\mathbf{r}_m,\omega)\ . \end{aligned} \tag{18}$$

In case of a multi-source/receiver experiment, let $\mathbf{r}_i^r$ and $\mathbf{r}_j^s$ represent respectively the location of receiver i and source j. Equation 18 is correspondingly replaced by matrices:

$$\begin{aligned} &\overline{R} = K\overline{E}, \quad \overline{R}^T = [p_s(\mathbf{r}_1^r,\omega), p_s(\mathbf{r}_2^r,\omega), \cdots, p_s(\mathbf{r}_N^r,\omega)] \\ &K = k_0^2(\mathbf{r}_m,\omega)O_m|\overline{G}_r||\overline{G}_s|\hat{G}_r^T\hat{G}_s, \quad \overline{E}^T = [1,1,\cdots,1]\ . \end{aligned} \tag{19}$$

The two vectors, $\overline{G}_r$ and $\overline{G}_s$, represent the following collection of Green's functions:

$$\overline{G}_r = |\overline{G}_r|\hat{G}_r = [G(\mathbf{r}_1^r,\mathbf{r}_m,\omega),\cdots,G(\mathbf{r}_N^r,\mathbf{r}_m,\omega)], \quad \overline{G}_s = |\overline{G}_s|\hat{G}_s = [G(\mathbf{r}_1^s,\mathbf{r}_m,\omega),\cdots,G(\mathbf{r}_M^s,\mathbf{r}_m,\omega)], \tag{20}$$

In practice, the system matrix K in Equation 19 is known from the measurements. This matrix has the dimension $N \times M$ and its singular value decomposition can be written formally as

$$K = [\overline{u}_1,\overline{u}_2,\cdots,\overline{u}_N] \begin{bmatrix} \lambda_1 & 0 & \cdots & 0 \\ 0 & \lambda_2 & \cdots & 0 \\ \cdots & \cdots & \cdots & \cdots \\ 0 & 0 & \cdots & \lambda_N \end{bmatrix} \begin{bmatrix} \overline{\nu}_1^{*T} \\ \overline{\nu}_2^{*T} \\ \cdots \\ \overline{\nu}_M^{*T} \end{bmatrix}\ . \tag{21}$$

Comparison between Equations 19 and 21 should give the expected eigenvalues:

$$\lambda_1 = k_0^2(\mathbf{r}_m,\omega)O_m|\overline{G}_r||\overline{G}_s|, \quad \lambda_2 = \lambda_3,\cdots,\lambda_N = 0\ . \tag{22}$$

Similarly, with respect to the singular functions one should expect:

$$\overline{u}_1 = \hat{G}_r^T, \quad \overline{\nu}_1^{*T} = \hat{G}_s\ . \tag{23}$$

Hence, the remaining singular functions represent the null-space of solutions with respect to both arrays. Because of the orthogonality between the singular functions, backpropagation of the null-space will give at the location of the scatterer:

$$\overline{G}_r^* \cdot \overline{u}_i = 0, \quad i = 2,3,\cdots,N, \qquad \overline{G}_s^* \cdot \overline{\nu}_i^*, \quad i = 2,3,\cdots,M\ . \tag{24}$$

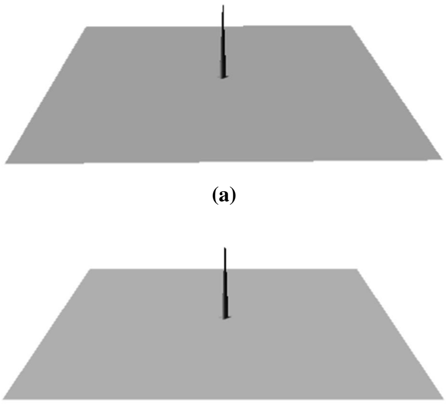

(a)

(b)

Figure 7: :'Super-resolved' point scatterer (half-ring aperture). (a) 5Hz and (b) 10 Hz.

By forming such null-space images employing all available singular functions, the final image will show a value close to zero at the position of the scatterer. By taking the inverse of this null-space image, a corresponding strong and narrow peak at the location of the scatterer will be obtained. Such a procedure is known as super-resolution in the literature (Lehman and Devaney, 2003).

Consider now a simple example to illustrate the power of this technique. In the simulations the same parameters are employed as in the example shown in Figure 6. However, in order to be able to apply SVD to the simulated data, another source was included. The position of the second source was in the same vertical (xz-)plane as the original source (cf. Figure 3) but this time displaced 200 m away from the scatterer along the negative z-axis. Figure 7 shows the result obtained by backpropagating the nil-space singular function associated with the receiver side. This 'super-resolved' image is to be compared with the corresponding ideal diffraction-limited image (focus) in Figures 6(b) or 6(e). Note that the result in Figure 7 was obtained using a *single frequency*. By analogy with conventional backpropagation addressed in the first part of this paper, singular function(s) representing the signal space can also be backpropagated employing a simple matched filtering approach (analogy with Equation 17b). However, if multiple frequencies are used to form an image, special care has to be taken. It is known that the singular vectors output from a SVD analysis of a complex-valued matrix system will be non-unique by an arbitrary phase; i.e. for one pair of left- and right-handed vectors it implies:

$$\overline{u}_i.e^{i\theta_i}, \quad \overline{\nu}_i.e^{i\theta_i} \tag{25}$$

with θ_i representing the non-unique phase. This non-uniqueness does not influence on the super resolution computations as given by Equation 24, since they are carried out per frequency, and the same applies if only a monochromatic image is computed based on the signal space singular vector(s). However, in case of multi-frequency imaging direct addition of the monochromatic sub images will give a distorted reconstruction. To obtain a focused image the magnitude of each sub image could be used. However, with respect to noise reduction it would be better to avoid the magnitude operation. In this paper, an alternative approach has been employed where each sub image is constrained so that it has the same phase in the centre of the scatterer. The final image obtained is shown in Figure 8 (two orthogonal views) and the limited aperture is reflected in the shape of the focus. As expected, the result in Figure 8 (left view) is similar to the one obtained in Figure 6(e). In this paper a single scatterer has been used as a demonstration case to analyze and further increase the basic understanding of both conventional backpropagation as used in migration as well as the concept of super resolution. Different from the classical backpropagation the latter approach is based on a decomposition of measurements into orthogonal signal- and noise-spaces. The more extensive discussion of multiple point scatterers and also extended targets fall outside the scope of this basic study. However, before closing this section a few comments will be made in connection with super resolution and multiple point-like targets. The extension to a case of L weak (Born) scatterers is rather straightforward, since such an ensemble will give rise to L linear scattering equations and correspondingly

(a) (b)

Figure 8: Image formed by backpropagating the signal space and adding the monochromatic sub images after phase corrections (two orthogonal views).

L non-zero eigenvalues. If M and/or $N > L$, the $M - L$ right-hand side and/or the $N - L$ left-hand side singular functions can be used for super-resolution' imaging' of this multi-scatterer case. Moreover, the first L eigenvalues correspond uniquely to one of the L scatterers. The underlying assumption is that the scatterers are fully resolved (ideal point-spread functions with respect to both source and receiver array), which mathematically can be stated as the conditions:

$$\overline{G}_r^*(i).\overline{G}_r^T(j) = 0, \quad \overline{G}_s^*(i).\overline{G}_s^T(j) = 0 \,, \quad i \neq j \,, \tag{26}$$

where $\overline{G}_s(i)$ and $\overline{G}_r(i)$ represent a Greens function vector with respect to respectively the source and the receiver array that focuses at a point scatterer located at the position $\mathbf{r}_i$. Equation 26 guarantees that the same Greens function vectors will form the singular functions associated with the scatterers. In case of strong scatterers there will no longer exist a one to one mapping between the non-zero eigenvalues and the scatterers. Instead, a given eigenvalue (and corresponding singular functions) will now represent a combination of several scatterers. Even if a SVD analysis can be employed the transition between signal and noise space will no longer be so sharp and also the extreme localization capability of the nil-solutions will degrade.

CONCLUDING REMARKS

This paper has provided a simple framework of understanding and analyzing both diffraction-limited imaging as well as super-resolution. Extrapolation of measurement data employing both the principles of migration and time-reversal give the same estimate of the scattered wavefields. In case of a point scatterer it is shown explicitly that the band-limited character of the focus is caused by a superimposition of converging and diverging waves. Hence, the backpropagation operation is non-causal by nature. Point-diffracted data can apparently be imaged beyond the diffraction-limit by making use of the null-space solutions. This concept applies equally to a single or a collection of scatterers as long as within the Born assumption (no interactions between scatterers). However, the apparently super-resolved focus has to be interpreted as an extreme localization rather than a quantitative image (the value of the peak is arbitrary). Possible extension of the idea to image segments (i.e. line of scatterers) should be further investigated. Future use of the concept can be within enhanced resolution of target zone changes associated with time-lapse data.

ACKNOWLEDGMENTS

This work has been partly funded by the Norwegian Science Foundation (NFR). Support of the members of the WIT Consortium is also acknowledged.

REFERENCES

Bakulin, A. and Calvert, R. (2006). The virtual source method: Theory and case study. *Geophysics*, 71:SI139–SI150.

Bojarski, N. N. (1983). Generalized reaction principles and reciprocity theorems for the waveequations, and the relationships between the time-advanced and time-retarded fields. *J. Acoust.Soc. Am.*, 74:281–285.

Born, M. and Wolf, E. (1999). *Principles of Optics*. Cambridge University Press, 7th Edition.

Esmersoy, C. and Oristaglio, M. (1988). Reverse-time wave-field extrapolation, imaging, and inversion. *Geophysics*, 53:920–931.

Fink, M. (1999). Time-reversal acoustics. *Scientific American Magazine*, November Issue.

Keller, J. B. (1987). Rays, waves and asymptotics. *Bull. Amer. Math. Soc.*, 84:727–751.

Langenberg, K. J. (1987). *Applied Inverse Problems for Acoustic, Electromagnetic, and Elastic Wave Scattering*, pages 125–467. *In* Basic Methods of Tomography and Inverse Problems, Ed. Sabatier, P.C., Adam Hilger Ltd.

Lehman, S. K. and Devaney, A. J. (2003). Transmission mode time-reversal super-resolution imaging. *J. Acoust. Soc. Am.*, 113:2742–2753.

Newton, R. G. (1982). *Scattering Theory of Waves and Particles*. Springer, 2nd Edition, New York.

Odendaal, J. W., Barnard, E., and Pistorius, C. W. I. (1994). Two-dimensional superresolution radar imaging using the music algorithm. *IEEE Transactions on Antennas and Propagation*, 42:1386–1391.

Prada, C., Kerbrat, E., Cassereau, D., and Fink, M. (2002). Time reversal techniques in ultrasonic nondestructive testing of scattering media. *Inverse Problems*, 18:1761–1773.

Rosny, J. and Fink, M. (2002). Overcoming the diffraction limit in wave physics using a time-reversal mirror and a novel acoustic sink. *Phys. Rev. Letters*, 89:124301–1 – 124301–4.

Schleicher, J., Tygel, M., and Hubral, P. (2007). *Seismic True-Amplitude Imaging*. Geophysical Developments Series No.12. Society of Exploration Geophysicists (SEG).

Schmidt, R. O. (1986). Multiple emitter location and signal parameter estimation. *IEEE Trans. Antennas Propagation*, AP-4:276–280.

Schneider, W. A. (1978). Integral formulation for migration in two and three dimensions. *Geophysics*, 43:49–76.

Scholz, B. (2002). Towards virtual electrical breast biopsy: space-frequency music for trans-admittance data. *IEEE Transactions on Medical Imaging*, 21:588–595.

Wapenaar, K. (2004). Retrieving the elastodynamic green's function of an arbitrary inhomogeneous medium by crosscorrelation. *Physical Review Letters*, 93:254301–1 – 254301–4.

Wiggins, J. W. (1984). Kirchhoff integral extrapolation and migration of nonplanar data. *Geophysics, 49, 1239-1248.*, 49:1239–1248.

APPENDIX A: THE LINK TO TIME-REVERSAL AND SEISMIC INTERFEROMETRY

By employing the principle of reciprocity of the Greens function, Equation 11 can be written on the alternative form:

$$\begin{aligned} &-\int_S \left[\frac{\partial G_0^*}{\partial n}(\mathbf{r}'', \mathbf{r}, \omega) G_0(\mathbf{r}'', \mathbf{r}'\omega) - G_0^*(\mathbf{r}'', \mathbf{r}, \omega)\frac{\partial G_0}{\partial n}(\mathbf{r}'', \mathbf{r}', \omega)\right] dS'' \\ &= G_0(\mathbf{r}, \mathbf{r}', \omega) - G_0^*(\mathbf{r}, \mathbf{r}', \omega) = G_0(\mathbf{r}', \mathbf{r}, \omega) - G_0^*(\mathbf{r}', \mathbf{r}, \omega)\ . \end{aligned} \tag{A-1}$$

which represents the time-reversal analogy (Fink, 1999) of Equation 11 (i.e. now with a point-source placed at $\mathbf{r}$). Equation A-1 can be interpreted as follows: the wave-field from a point source at $\mathbf{r}$ is measured along the surface S. These measurements are then time-reversed (which corresponds to the operation of complex conjugating in the frequency domain) and forward propagated to obtain a focus. Comparison between Equations 11 and A-1 shows that the basic operation of backpropagation within a migration formulation or a time-reversal formulation gives the same diffraction-limited image. In case of an incomplete coverage the focus will be even more distorted as demonstrated in Figure 6.

Also by employing reciprocity Equation 11 can be transformed to another alternative form with a new physical interpretation:

$$\begin{aligned}&-\int_S \left[\frac{\partial G_0^*}{\partial n}(\mathbf{r},\mathbf{r}'',\omega)G_0(\mathbf{r}',\mathbf{r}''\omega) - G_0^*(\mathbf{r},\mathbf{r}'',\omega)\frac{\partial G_0}{\partial n}(\mathbf{r}',\mathbf{r}'',\omega)\right] dS'' \\ &= G_0(\mathbf{r},\mathbf{r}',\omega) - G_0^*(\mathbf{r},\mathbf{r}',\omega)\ . \end{aligned} \qquad \text{(A-2)}$$

Equation A-2 serves as the starting point of seismic interferometry (Wapenaar, 2004) and the closely-related concept of virtual-source imaging (Bakulin and Calvert, 2006). This can be more easily seen if the high-frequency and far-field version of Equation A-2 is employed:

$$2i\int_S k_0(\mathbf{r}'',\omega)\left[G_0^*(\mathbf{r},\mathbf{r}'',\omega)G_0(\mathbf{r}',\mathbf{r}'',\omega)\right] dS'' = G_0(\mathbf{r},\mathbf{r}',\omega) - G_0^*(\mathbf{r},\mathbf{r}',\omega)\ . \qquad \text{(A-3)}$$

Realize first that the operation under the integral represents a cross-correlation in the frequency-domain. The physical interpretation is now as follows: the contributions from active sources distributed over the surface S are measured at two receiver positions $\mathbf{r}$ and $\mathbf{r}'$. Cross-correlation of these data (left-hand side) transforms one of the receivers to a virtual source (cf. right-hand side) as discussed by Bakulin and Calvert (2006). Alternatively, by assuming random underground sources (associated with reservoir production as an example), Equation A-3 can be used to transform passive seismic surface recordings to active experiments (Wapenaar, 2004). This is known as seismic interferometry in the literature.

APPENDIX B: HIGH-FREQUENCY LIMIT OF THE KERNEL B - GENERAL MODEL AND IDEAL APERTURE

The kernel B is defined in Equation 11. Integration over available frequency band gives:

$$\int_\omega B(\mathbf{r},\mathbf{r}',\omega)d\omega = -\int_\omega\int_S \left[\frac{\partial G_0^*}{\partial n}(\mathbf{r},\mathbf{r}'',\omega)G_0(\mathbf{r}'',\mathbf{r}'\omega) - G_0^*(\mathbf{r},\mathbf{r}'',\omega)\frac{\partial G_0}{\partial n}(\mathbf{r}'',\mathbf{r}',\omega)\right] dS''d\omega\ . \qquad \text{(B-1)}$$

Introduce the high-frequency approximation and represent the Green's functions by:

$$\begin{aligned} G_0^*(\mathbf{r},\mathbf{r}'',\omega) &= a(\mathbf{r},\mathbf{r}'')e^{i\omega\tau(\mathbf{r},\mathbf{r}'')}, \\ G_0(\mathbf{r}'',\mathbf{r}',\omega) &\approx a(\mathbf{r},\mathbf{r}'')e^{i\omega[\tau(\mathbf{r},\mathbf{r}'')+\nabla\tau(\mathbf{r},\mathbf{r}'')\cdot(\mathbf{r}'-\mathbf{r})]}, \end{aligned} \qquad \text{(B-2)}$$

Next, assume far-field configuration and let S represent the wavefront surface at infinity due to a source located at $\mathbf{r}$. Hence, the normal derivative terms in Equation B-1 can be evaluated on the wavefront surface S by using (c_0 being the velocity along the surface):

$$\frac{\partial}{\partial n} = \frac{1}{c_0(\mathbf{r}'')}\frac{\partial}{\partial\tau}\ . \qquad \text{(B-3)}$$

Combination of Equations B-1-B-3 gives the far-field and high-frequency approximation of the kernel:

$$\int_\omega B(\mathbf{r},\mathbf{r}',\omega)d\omega = \int_\omega\int_S \frac{2i\omega a^2(\mathbf{r},\mathbf{r}'')}{c_0(\mathbf{r}'')}e^{i\omega\nabla\tau(\mathbf{r},\mathbf{r}'')\cdot(\mathbf{r}'-\mathbf{r})}dS''d\omega\ . \qquad \text{(B-4)}$$

Assume that a unity sphere is surrounding the point $\mathbf{r}$ (e.g. $|\hat{\nu}| = 1$ in Figure 9). Conservation of energy within the ray tube gives the relationship Keller (1987):

$$\frac{a^2(\mathbf{r},\mathbf{r}'')}{c_0(\mathbf{r}'')}d\mathbf{r}'' = \frac{a^2(\mathbf{r},\hat{\boldsymbol{\nu}})}{c_0(\hat{\boldsymbol{\nu}})}d\hat{\boldsymbol{\nu}}\ . \qquad \text{(B-5)}$$

with the spherical coordinate system defined by

$$\hat{\boldsymbol{\nu}} = \sin\nu_1\cos\nu_2\hat{\mathbf{i}} + \sin\nu_1\sin\nu_2\hat{\mathbf{j}} + \cos\nu_2\hat{\mathbf{k}}, \quad d\hat{\boldsymbol{\nu}} = \sin\nu_1 d\nu_1 d\nu_2\ . \qquad \text{(B-6)}$$

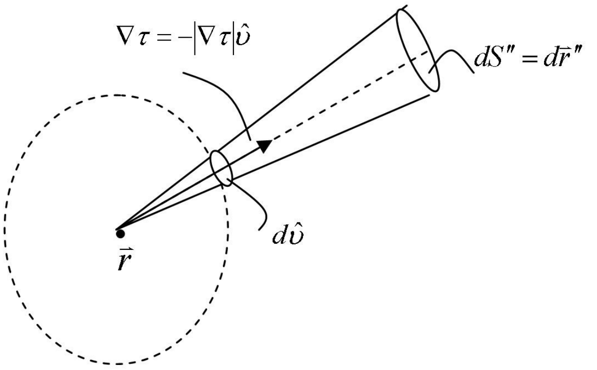

Figure 9: Ray tube defining coordinate transformation.

Assuming a homogenous medium within the infinitesimal sphere it follows that (spherical wave):

$$a(\mathbf{r}, \hat{\boldsymbol{\nu}}) = \frac{1}{4\pi} , \tag{B-7}$$

and also that

$$c_0(\hat{\boldsymbol{\nu}}) = c_0(\mathbf{r}) . \tag{B-8}$$

Combination of Equations B-4, B-5, B-7 and B-8 gives (also making use of the fact that $\nabla\tau(\mathbf{r}, \mathbf{r}'') = -\frac{1}{c_0(\mathbf{r})}\hat{\boldsymbol{\nu}}$):

$$\int_\omega B(\mathbf{r}, \mathbf{r}', \omega)d\omega = \frac{1}{(4\pi)^2}\int_\omega \int_S \frac{2i\omega}{c_0(\mathbf{r})} e^{-i\omega\hat{\boldsymbol{\nu}}\cdot(\mathbf{r}'-\mathbf{r})/c_0(\mathbf{r})} d\hat{\boldsymbol{\nu}} d\omega . \tag{B-9}$$

In this derivation the following assumptions have been employed:

- A locally homogeneous volume surrounds the point-source located at $\mathbf{r}$.
- All points $\mathbf{r}'$ considered are close to $\mathbf{r}$ (in accordance with Equation B-2).

Hence, very close to the point-source focus Equation B-9 should be omnidirectional. Consequently, one may set $\boldsymbol{\nu} \cdot (\mathbf{r}' - \mathbf{r}) = |\mathbf{r}' - \mathbf{r}|$ in Equation B-9, implying that it can be further simplified as:

$$\int_\omega B(\mathbf{r}, \mathbf{r}', \omega)d\omega = \frac{1}{4\pi c_0}\int_{\omega=-\infty}^{\infty} i\omega\; e^{-i\omega|\mathbf{r}'-\mathbf{r}|/c_0(\mathbf{r})}d\omega = \frac{\delta(|\mathbf{r}' - \mathbf{r}|/c_0(\mathbf{r}))}{4\pi|\mathbf{r}' - \mathbf{r}|} , \tag{B-10}$$

which is consistent with Equation 15.